



# Axi symmetric 2D simulation and numerical heat transfer characteristics for the calibration furnace in a rectangular enclosure

Sudhakar Matle\*, S. Sundar<sup>1</sup>

Department of Mathematics, IIT Madras, Chennai 600 036, India

## ARTICLE INFO

### Article history:

Received 5 May 2010

Received in revised form 15 June 2011

Accepted 11 July 2011

Available online 22 July 2011

### Keywords:

Rectangular enclosure

Simulation

Mesh sensitivity

Numerical uncertainty

## ABSTRACT

This paper presents axi symmetric 2D numerical investigation of the spherical thermocouple calibration furnace in a rectangular enclosure. The focus is on the flow structure inside the Saturn (a hollow spherical cavity), external flow behavior due to annulus block heating and the surface temperature uniformity. Mesh sensitivity analysis is adopted to extract the mesh with minimum number of nodes but with fast convergent finite element solution. The basic strategy here is that temperature perturbation error at a single point instead of a single element contributed to the total perturbation error qualitatively remains the same. Agreement between numerical simulation results and the experiment results is good with a maximum temperature deviation 10 °C for the cavity temperature 400 °C. Finally, standard numerical temperature uncertainty due to variation in thermal conductivity is computed through the sensitivity coefficient using uncertainty analysis.

© 2011 Elsevier Inc. All rights reserved.

## 1. Introduction

Calibration of radiation thermometers [1] is one of the important research activities in the field of metrology. Calibration is an act of adjusting instrument by comparison against standard. Radiation thermometers are calibrated using a standard surface of known temperature. The Saturn surface is one of such standards used in the calibration. The Saturn is a hollow spherical cavity embedded in the calibration furnace. The important advantage for choosing the spherical cavity is that the cavity behaves like a black body (emissivity  $\epsilon$  is almost 1) despite the fact that it is a grey body. Hence, more accuracy is achieved in the emitted radiation measured by radiation thermometer. Radiation thermometers are sighted at the inner surface of the spherical cavity through the furnace aperture (see Fig. 1).

Calibration furnace (see Fig. 1) consists of six concentric layers and each layer is embedded in the other. The first outermost layer is in steel having a thickness of 0.02 m. Inside this layer, a ceramic fibre is established over the entire annulus of diameter 0.051 m to avoid heat losses. Ceramic fibre envelopes the annulus block heating which consists of helicoidal copper coil with best thermal properties arranged internally to the cement block. Copper coil is formed like a serpentine spread through all zones interior to the block. Power supply is provided to the copper coil through the small gaps in layers. Inside this block heating, there is another ceramic fibre envelopes the spherical cavity to withstand elevated temperatures.

Nine calibrated positions marked as F1, F2, F3, F4, F5, C6, C7, C8 and C9 are selected for temperature measurement on the spherical cavity surface and they are sketched systematically in Fig. 2. F1 is marked exactly opposite to the frontal diameter of the spherical cavity. Positions F2, F3, F4 and F5 are indicated on the surface cross section so that they are on the same side (opposite to frontal view) and they are on the same circle. This cross sectional surface cut makes a solid angle of 30Sr at the

\* Corresponding author. Tel.: +91 9790951093.

E-mail addresses: [iitsudha@gmail.com](mailto:iitsudha@gmail.com) (S. Matle), [slnt@iitm.ac.in](mailto:slnt@iitm.ac.in) (S. Sundar).

<sup>1</sup> Tel.: +91 44 22574608.

### Nomenclature

$r, z$	cylindrical coordinates
$R, Z$	dimensionless coordinates in $r$ -, $z$ -directions
$U, V$	dimensionless velocities in $r$ -, $z$ -directions
$T_s$	surface temperature ( $^{\circ}\text{C}$ )
$T_{amb}$	ambient temperature ( $^{\circ}\text{C}$ )
$L$	characteristic length (length of the layer or diameter of the sphere)
$AR$	aspect ratio (width to height ratio)
$Ra$	Rayleigh number $= \frac{g\beta\Delta T L^3}{\nu\alpha}$
$Nu_{loc}$	local Nusselt number $= \frac{hR}{k}$
$k$	thermal conductivity ( $\text{W/m K}$ )
$Pr$	Prandtl number ( $=0.71$ at $T_{ref} = 20^{\circ}\text{C}$ )
$\mathbf{n}$	unit normal vector
$\mathbf{E}$	number of elements
$\mathbf{N}$	number of nodes
$h$	maximum element size (length of largest edge in an element) (m)
$h$	convective heat transfer coefficient ( $\text{W/m}^2 \text{K}$ )

### Greeks

$\phi$	azimuthal angle
$\rho$	density of the air ( $\text{kg/m}^3$ )
$\alpha$	thermal diffusivity ( $\text{m}^2/\text{s}$ )
$\beta$	coefficient of volumetric thermal expansion ( $1/^{\circ}\text{C}$ )
$\epsilon$	emissivity of the cavity
$\theta$	dimensionless temperature
$\sigma$	Stefan Boltzmann constant ( $5.67 \times 10^{-8} \text{W/m}^2 \text{K}^4$ )

center of the spherical cavity. Positions C6, C7, C8 and C9 are selected on the great circle so that none of them comes at the frontal side. In an experiment, the measured surface temperature at nine thermocouple positions are not the same for a particular cavity temperature.

An important requirement for calibration of radiation thermometers is that the cavity must be isothermal ( $\Delta T = 0, Q \neq 0$ ). But it is difficult to maintain isothermal character for the spherical cavity although uniform heating provided. This is the drawback of the experiment and consequently results might be inaccurate. Reason being (1) heat losses due to the aperture (2) heat losses due to air gaps in the ceramic material. In order to understand thoroughly, it is essential to study behavior of temperature profile for particular aperture size of the spherical cavity. If the aperture size is large, heat radiation cannot produce sufficient number of reflections required to increase the cavity emissivity. Cavity emissivity against the surface temperature uniformity plot determines the heat dissipation rate through the aperture. The developed mathematical model and then numerical simulation gives better insight and understanding of the experiment, optimize uncertainties in the solution that suggest a methodology to improve quality of the equipment.

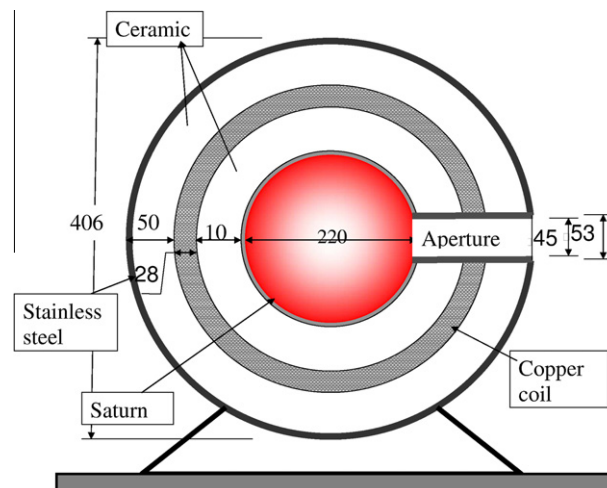
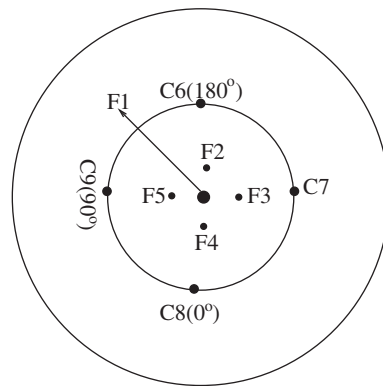


Fig. 1. Calibration furnace (dimensions expressed in mm).



**Fig. 2.** 2D pictorial representation of thermocouple positions on the surface of the spherical cavity (opposite to frontal view wherein the aperture placed).

Many research efforts have been done on finite element modeling [2–4] of calibration furnaces, industrial furnaces and solar cavity receivers for quality equipment. Recently, Oluwole et al. [5] studied the heat flow patterns in two salt bath furnaces using finite element analysis. The implications of the heat flows on long term stability of furnace performance were evaluated.

Fournier et al. [6] presented the application of spectral finite element method to model axi symmetric flows in rapidly rotating domains. Chan et al. [7] investigated implementation of finite element method to solve the spherical kinematic dynamo problem. The time dependent and static Maxwell equations in axi symmetric singular domains were studied in Assoum et al. [8,9] by introducing a method based on a splitting of space of solutions into a regular subspace and a singular one. Bermudez et al. [10,11] provided rigorous mathematical analysis of finite element method used to underlying electromagnetic model and thermal model.

A review of literature on mesh sensitivity analysis shows that this concept was the object of numerous numerical simulation studies. Among the recent investigations included are; Li et al. [12] developed a structured adaptive mesh refinement (SAMR) method for parabolic differential equation systems, Becker and Vexler [13,14] explained numerical sensitivity analysis and mesh refinement for calibration of parameters using a posteriori error bounds. These error estimators are used in an adaptive algorithm to construct economic meshes by local mesh refinement. Gratsch and Bathe [15] reviewed the basic concepts of a posteriori error estimators in finite element method applications. Nithiarasu and Zienkiewicz [16] had explained in their paper, adaptive mesh generation techniques for fluid mechanics problems based on a coarser mesh. In another study, Kuznik and Rusaouen [17] employed four different non uniform grids to study the grid independence and accuracy of the method.

Research efforts have been expanded to free convection heat transfer from a heated sphere in non Newtonian fluids and Newtonian fluids [18–22]. Yang et al. [23] discretized the full Navier–Stokes equations and the energy equation for laminar natural convection heat transfer over an isothermal sphere using the finite control volume formulation and solved by employing the SIMPLEC method. Natural convection within enclosures [24–28] has an obvious applications to heat loss from furnaces [29], buildings and solar cavity receivers. Anderson and Lauriat [30] conducted a numerical study of natural convection in a closed cavity with an isothermal vertical wall and a heated floor.

Chen and Wang [31] correlated Nusselt number as a function of Rayleigh number and the aspect ratio (AR) and compared results of the isothermal elliptic cavity with results of Elsayed et al. [32]. Bejan and Tien [33] have been done the analysis of natural convection in a shallow enclosure and extended analysis for complicated enclosure problems [34].

The publication of the guide to the expression of uncertainty in measurement (GUM) [35] was the product of the need for international consensus for the expression of uncertainty in measurement endorsed by the International Bureau of Weights and Standards, the International Electrotechnical Commission, the International Federation of Clinical Chemistry, the International Organization for Standardization, the International Union of Pure and Applied Chemistry, the International Union of Pure and Applied Physics, and the International Organization of Legal Metrology. Drnovsek et al. [36] discussed and defined the total uncertainty in temperature calibrations by comparison, and by analyzing the propagated errors.

In the next section, the actual problem, governing equations and corresponding boundary conditions are discussed. In Section 3, finite element formulation and then numerical simulation are presented. In Section 4, mesh sensitivity analysis using local mesh refinement method, surface temperature uniformity, free convection characteristics of the isothermal Saturn surface and calculations of the standard numerical temperature uncertainty on the isothermal cavity surface are thoroughly presented.

## 2. Problem

The spherical furnace is kept in a rectangular enclosure with the uniform block heating. The size of the enclosure under numerical investigation is approximately ten times smaller than the enclosure used in the experiment. It is notified that the

enclosure effects beyond the scope of the paper. Due to the symmetry and the isothermal character of the spherical furnace, the left half part of it is considered for numerical investigation. There is no consideration of the furnace aperture and its effect on the spherical cavity surface through out the numerical study.

2.1. Mathematical model

The computational domain ( $\Omega$ ) is assumed to be union of the two sub domains  $\Omega_1$  (gas) and  $\Omega_2$  (solid). The schematic sketch of the computational domain is shown in Fig. 3. The revolution of  $\Omega$  around the axis of symmetry gives rise to full 3D domain. The computational domain is fixed in between the left side with coordinates  $[(-0.3, -0.273), (-0.3, 0.4)]$  and the right side with coordinates  $[(0, -0.273)$  and  $(0, 4)]$ . Concentric sub domains are established with settings from the outermost to the innermost: stainless steel (44.5 W/m K), ceramic ( $\text{SiO}_2$ ) (1.4 W/m K), concrete (1.8 W/m K), copper (400 W/m K) and ceramic ( $\text{SiO}_2$ ). The value in parentheses is the thermal conductivity of the corresponding material. The innermost sub domain is filled with air at Boussinesq. 20 °C.

2.2. Governing equations

We assume the flow is incompressible and steady. In fact, the steady state results are considered in the experiment. Flow is generated by temperature variation which leads to local density differences. Therefore, the body force is added to include the effect of local density differences. Hence, the Boussinesq approximation employed is,

$$g(\rho - \rho_{amb}) = g\beta(T - T_{amb}), \tag{1}$$

where  $g$  is acceleration due to gravity ( $9.81 \text{ m/s}^2$ ) and  $\beta$  is coefficient thermal expansion. The partial differential equations which govern the flow are the steady state incompressible Navier–Stokes equations

$$\begin{aligned} \rho(\mathbf{u} \cdot \nabla)\mathbf{u} &= \nabla \cdot \left[ (-pI + \mu(\nabla\mathbf{u} + (\nabla\mathbf{u})^T)) \right] + g\beta(T - T_{amb}) \text{ in } \Omega_1, \\ \nabla \cdot \mathbf{u} &= 0 \text{ in } \Omega_1, \end{aligned} \tag{2}$$

where  $\rho$  is the density and  $\mu$  is the dynamic viscosity. The buoyancy force term  $g\beta(T_s - T_{amb})$  is added to the momentum equation in the gravity direction and  $\Omega_1$  is the bounded air region.  $\mathbf{u}$  is natural convection velocity and  $p$  is hydrostatic pressure. The steady state heat energy equations which govern the heat transfer as follows:

$$\begin{aligned} \nabla \cdot (-k\nabla T) &= Q - \rho C_p \mathbf{u} \cdot \nabla T \text{ in } \Omega_1, \\ \nabla \cdot (-k\nabla T) &= Q \text{ in } \Omega_2, \end{aligned} \tag{3}$$

where  $T$  is the temperature,  $k$  is the thermal conductivity,  $C_p$  is the specific heat capacity at constant pressure (101,325 Pa) and  $Q$  is the heat source provided, zero everywhere except in the copper region. The term  $\mathbf{u} \cdot \nabla T$  represents convective term while the term  $\nabla \cdot (-k\nabla T)$  represents thermal diffusivity. The revolution of axi symmetric 2D domain around the axis of symmetry gives rise to the full 3D domain. For an axi symmetric 2D problem, governing equations in cylindrical coordinates  $(r, \phi, z)$ ,  $\phi = 0$ , with origin  $(0, 0, 0)$  as follows:

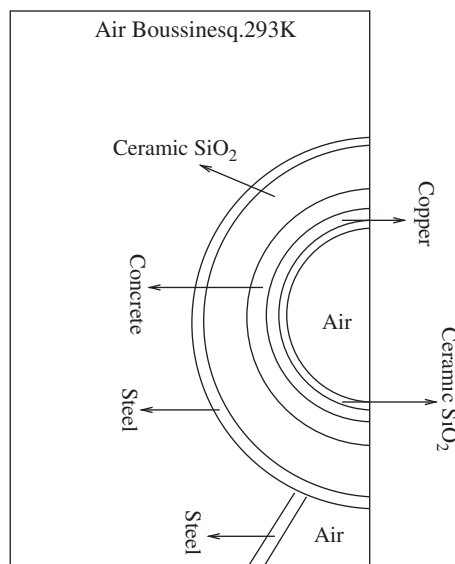


Fig. 3. A schematic of the computational geometry and domain settings.

$$\frac{1}{r} \frac{\partial(ru_r)}{\partial r} + \frac{\partial u_z}{\partial z} = 0,$$

$$u_r \frac{\partial u_r}{\partial r} + u_z \frac{\partial u_r}{\partial z} = -\frac{1}{\rho} \frac{\partial p}{\partial r} + \nu \left( \frac{1}{r} \frac{\partial(r \frac{\partial u_r}{\partial r})}{\partial r} + \frac{\partial^2 u_r}{\partial z^2} \right), \tag{4}$$

$$u_r \frac{\partial u_z}{\partial r} + u_z \frac{\partial u_z}{\partial z} = -\frac{1}{\rho} \frac{\partial p}{\partial z} + \nu \left( \frac{1}{r} \frac{\partial(r \frac{\partial u_z}{\partial r})}{\partial r} + \frac{\partial^2 u_z}{\partial z^2} \right) + g\beta(T - T_{amb}),$$

$$u_r \frac{\partial T}{\partial r} + u_z \frac{\partial T}{\partial z} = \alpha \left[ \frac{1}{r} \frac{\partial(r \frac{\partial T}{\partial r})}{\partial r} + \frac{\partial^2 T}{\partial z^2} \right] + \frac{Q}{\rho C_p} \frac{1}{r} \frac{\partial(r \frac{\partial T}{\partial r})}{\partial r} + \frac{\partial^2 T}{\partial z^2} + \frac{Q}{k} = 0, \tag{5}$$

where  $\nu = \frac{\mu}{\rho}$  is the viscous coefficient and  $\alpha = \frac{k}{\rho C_p}$  is the coefficient of thermal diffusivity.

2.3. Non-dimensional analysis

$$\frac{1}{R} \frac{\partial(RU_R)}{\partial R} + \frac{\partial U_Z}{\partial Z} = 0,$$

$$U_R \frac{\partial U_R}{\partial R} + U_Z \frac{\partial U_R}{\partial Z} = -\frac{\partial P}{\partial R} + Pr \left( \frac{1}{R} \frac{\partial(R \frac{\partial U_R}{\partial R})}{\partial R} + \frac{\partial^2 U_R}{\partial Z^2} \right), \tag{6}$$

$$U_R \frac{\partial U_Z}{\partial R} + U_Z \frac{\partial U_Z}{\partial Z} = -\frac{\partial P}{\partial Z} + Pr \left( \frac{1}{R} \frac{\partial(R \frac{\partial U_Z}{\partial R})}{\partial R} + \frac{\partial^2 U_Z}{\partial Z^2} \right) + Ra Pr \theta,$$

$$U_R \frac{\partial \theta}{\partial R} + U_Z \frac{\partial \theta}{\partial Z} = \frac{1}{R} \frac{\partial(R \frac{\partial \theta}{\partial R})}{\partial R} + \frac{\partial^2 \theta}{\partial Z^2} + \mathbf{Q}_L \frac{1}{R} \frac{\partial(R \frac{\partial \theta}{\partial R})}{\partial R} + \frac{\partial^2 \theta}{\partial Z^2} + \mathbf{Q}_L = 0, \tag{7}$$

where  $R = \frac{r}{L}; Z = \frac{z}{L}$  are cylindrical coordinates in dimensionless form when the azimuthal angle  $\phi = 0$ . 'L' is the characteristic length. In the absence of a reference velocity value, dimensionless scales adopted for natural convection velocities are  $U_R = \frac{u_r L}{\alpha}$  and  $U_Z = \frac{u_z L}{\alpha}$ . In addition to this, dimensionless pressure  $P = \frac{\rho L^2}{\rho \alpha^2}$  and dimensionless temperature  $\theta = \frac{T - T_{amb}}{T_s - T_{amb}}$  are the other scales. Substitution of these dimensionless scales in (4) result in dimensionless parameters: Rayleigh number  $Ra = \frac{g\beta\Delta T L^3}{\nu\alpha} = \frac{g\beta\Delta T L^3 \rho^2 C_p}{\mu k}$ , Prandtl number  $Pr = \frac{\nu}{\alpha} = \frac{\mu C_p}{k}$  and  $\mathbf{Q}_L = \frac{Q L^2}{k(T_s - T_{amb})}$ . It is important to note that  $\mathbf{Q}_L$  is zero everywhere except in the copper conduction region. Here 'T<sub>s</sub>' is the surface temperature while 'T<sub>amb</sub>' is temperature in the ambient medium. Prandtl number is taken as 0.71 for air at room temperature 20 °C. For  $Ra > Ra_c = 265$ , the nature of heat transfer changed from conduction to convection when  $T_s = 400$  °C.

2.4. Boundary conditions

The boundary conditions for an axi symmetric 2D computational domain are sketched in Fig. 4. In general, no slip conditions on the solid interior boundaries of the computational domain. Continuity condition is considered when the heat is transported through conduction while convective and radiative conditions are employed at the solid and the fluid interface.

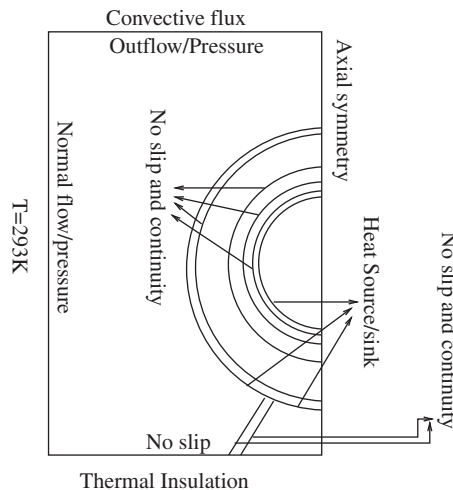


Fig. 4. A schematic boundary conditions for the computational domain.

Thermal insulation is considered at boundaries when the heat flux is zero. Normal flow/pressure and  $T = T_{ref} = 20^\circ\text{C}$  at the boundary where the flow is normal and the temperature is room temperature. Convective flux and outflow/pressure are considered at the boundary where convective air is moving vertical direction due to buoyancy.

Flow boundary conditions considered for the computational domain ( $\Omega_1$ ): normal flow or pressure at the left, out flow or pressure at the top, axi-symmetry at the right, no slip at the bottom and at the boundary common to  $\Omega_1$  and  $\Omega_2$ . The heat transport boundary conditions employed on the computational domain ( $\Omega$ ):  $T = T_{ref} = 20^\circ\text{C}$  at the left, convective flux at the top, thermal insulation at the bottom, axial symmetry at the right and continuity is considered at interior boundaries except at the innermost boundary and at the outermost boundary of the modeled furnace.

### 3. Finite element formulation and numerical simulation

We introduce function spaces  $X \subset H_0^1(\Omega_1)$ ,  $M \subset L_1^2(\Omega_1)$  and  $Y \subset H_0^1(\Omega)$  for velocity  $\mathbf{u} \in X$ , pressure  $p \in M$  and temperature  $T \in Y$ . The space of square integrable functions  $L_1^2(\Omega)$  (see [37]) is given by

$$L_1^2(\Omega) = \left\{ w : \Omega \rightarrow k, k \text{ real}, \|w\| = \left( \int_{\Omega} w^2 d\Omega \right)^{\frac{1}{2}} < \infty \right\}. \quad (8)$$

The associated inner product is  $(f, g) = \int_{\Omega} fg d\Omega$ ,  $\forall (f, g) \in L_1^2(\Omega) \times L_1^2(\Omega)$ .

The 2-D weighted Sobolov space  $H_1^1(\Omega)$  and its induced norm are defined as follows.

$$H_1^1(\Omega) = \left\{ w \in L_1^2(\Omega), \frac{\partial w}{\partial r} \in L_1^2(\Omega), \frac{\partial w}{\partial z} \in L_1^2(\Omega) \right\} \quad (9)$$

$$\|w\|_2^2 = \int_{\Omega} \left( w^2 + \left( \frac{\partial w}{\partial r} \right)^2 + \left( \frac{\partial w}{\partial z} \right)^2 \right) d\Omega.$$

The components of velocity ( $u_r, 0, u_z$ ) and components of the temperature ( $T_r, 0, T_z$ ) have to satisfy axial symmetric boundary condition

$$u_r = T = 0, \quad \frac{\partial u_z}{\partial z} = 0, \quad \frac{\partial T}{\partial z} = 0, \quad (10)$$

$$W_1^1(\Omega) = \{w \in H_1^1(\Omega), w = 0 \text{ on the axial symmetry}\}, \quad (11)$$

$$W_{10}^1(\Omega) = \{w \in W_1^1(\Omega), w = 0 \text{ on the entire boundary}\}.$$

Then the space of admissible velocities and admissible temperatures and the space of weight functions are as follows:

$$H^1(\Omega) = W^1(\Omega) \times W^1(\Omega) \times H_1^1(\Omega), \quad (12)$$

$$H_0^1(\Omega) = W_{10}^1(\Omega) \times W_{10}^1(\Omega) \times H_{10}^1(\Omega).$$

Since no boundary condition is prescribed on the pressure field, the space of pressure weight functions is the same as the space of pressure basis functions and consists simply of the space of square integrable functions defined over  $\Omega_1$ . The weak formulation of continuity and the momentum equations then takes the following form: find  $(u_r, 0, u_z, p) \in H^1(\Omega) \times L_1^2(\Omega_1)$  with  $\mathbf{u} - \mathbf{u}_b \in H_0^1(\Omega_1)$ , such that

$$\int_{\Omega} q \left[ \frac{1}{r} \frac{\partial(ru_r)}{\partial r} + \frac{\partial u_z}{\partial z} \right] = 0 \quad \forall q \in L_1^2(\Omega_1), \quad (13)$$

$$\int_{\Omega} w \left( u_r \frac{\partial u_r}{\partial r} + u_z \frac{\partial u_r}{\partial z} \right) d\Omega - \int_{\Omega} wv \left( \frac{1}{r} \frac{\partial(r \frac{\partial u_r}{\partial r})}{\partial r} + \frac{\partial^2 u_r}{\partial z^2} - \frac{u_r}{r^2} \right) d\Omega + \int_{\Omega} w \frac{1}{\rho} \frac{\partial p}{\partial r} d\Omega = 0 \quad \forall w \in H_0^1(\Omega_1), \quad (14)$$

$$\int_{\Omega} w \left( u_r \frac{\partial u_z}{\partial r} + u_z \frac{\partial u_z}{\partial z} \right) d\Omega - \int_{\Omega} wv \left( \frac{1}{r} \frac{\partial(r \frac{\partial u_z}{\partial r})}{\partial r} + \frac{\partial^2 u_z}{\partial z^2} \right) d\Omega + \int_{\Omega} w \frac{1}{\rho} \frac{\partial p}{\partial z} d\Omega = 0 \quad \forall w \in H_0^1(\Omega_1).$$

The weak form of the heat energy equation is as follows: find  $T \in H^1(\Omega)$  such that

$$\int_{\Omega} s_1 \left( u_r \frac{\partial T}{\partial r} + u_z \frac{\partial T}{\partial z} \right) d\Omega - \int_{\Omega} s_1 \alpha \left( \frac{1}{r} \frac{\partial(r \frac{\partial T}{\partial r})}{\partial r} + \frac{\partial^2 T}{\partial z^2} \right) d\Omega + \int_{\Omega} s_1 \frac{Q}{\rho C_p} d\Omega = 0 \quad \forall s_1 \in H_0^1(\Omega_1), \quad (15)$$

$$\int_{\Omega} s_2 \left( \frac{1}{r} \frac{\partial(r \frac{\partial T}{\partial r})}{\partial r} + \frac{\partial^2 T}{\partial z^2} \right) d\Omega - \int_{\Omega} s_2 \frac{Q}{k} d\Omega = 0 \quad \forall s_2 \in H_0^1(\Omega_2).$$

Application of divergence theorem to the diffusive term and using the condition  $w = 0$  on the boundary of the domain, the weak formulation for (13)–(15) is written as follows. Find  $(u_r, 0, u_z, p) \in H^1(\Omega) \times L^2_1(\Omega_1)$  with  $\mathbf{u} - \mathbf{u}_b \in H^1_0(\Omega_1)$ , such that

$$\int_{\Omega} q \left[ \frac{1}{r} \frac{\partial(ru_r)}{\partial r} + \frac{\partial u_z}{\partial z} \right] = 0 \quad \forall q \in M, \quad (16)$$

$$\begin{aligned} \int_{\Omega} w \left( u_r \frac{\partial u_r}{\partial r} + u_z \frac{\partial u_r}{\partial z} \right) d\Omega - \int_{\Omega} v \frac{1}{r} \frac{\partial w}{\partial r} \left( r \frac{\partial u_r}{\partial r} \right) + \frac{\partial w}{\partial z} \frac{\partial u_r}{\partial z} - \frac{u_r}{r^2} d\Omega + \int_{\Omega} w \frac{1}{\rho} \frac{\partial p}{\partial r} d\Omega = 0 \quad \forall w \in X, \\ \int_{\Omega} w \left( u_r \frac{\partial u_z}{\partial r} + u_z \frac{\partial u_z}{\partial z} \right) d\Omega - \int_{\Omega} v \left( \frac{1}{r} \frac{\partial w}{\partial r} \left( r \frac{\partial u_z}{\partial r} \right) + \frac{\partial w}{\partial z} \frac{\partial u_z}{\partial z} \right) d\Omega + \int_{\Omega} w \frac{1}{\rho} \frac{\partial p}{\partial z} d\Omega \\ - \int_{\Omega} w g \beta (T - T_{amb}) d\Omega = 0 \quad \forall w \in X. \end{aligned} \quad (17)$$

The weak formulation of (15) as follows: find  $T \in H^1(\Omega)$  such that

$$\begin{aligned} \int_{\Omega} s_1 \left( u_r \frac{\partial T}{\partial r} + u_z \frac{\partial T}{\partial z} \right) d\Omega + \int_{\Omega} \alpha \left( \frac{1}{r} \frac{\partial s_1}{\partial r} \left( r \frac{\partial T}{\partial r} \right) + \frac{\partial s_1}{\partial z} \frac{\partial T}{\partial z} \right) d\Omega + \int_{\Omega} s_1 \frac{Q}{\rho C_p} d\Omega = 0 \quad \forall s_1 \in Y, \\ \int_{\Omega} \left( \frac{1}{r} \frac{\partial s_2}{\partial r} \left( r \frac{\partial T}{\partial r} \right) + \frac{\partial s_2}{\partial z} \frac{\partial T}{\partial z} \right) d\Omega + \int_{\Omega} s_2 \frac{Q}{k} d\Omega = 0 \quad \forall s_2 \in Y. \end{aligned} \quad (18)$$

Compact version for the integral forms defined in (16)–(18) as follows:

$$\begin{aligned} d(\mathbf{u}, q) &= - \int_{\Omega_1} q \nabla \cdot \mathbf{u} d\Omega, \\ a(w; u_r) &= \int_{\Omega_1} v \left( \frac{1}{r} \frac{\partial w}{\partial r} \left( r \frac{\partial u_r}{\partial r} \right) + \frac{\partial w}{\partial z} \frac{\partial u_r}{\partial z} \right) d\Omega, \\ a(w; u_z) &= \int_{\Omega_1} v \left( \frac{1}{r} \frac{\partial w}{\partial r} \left( r \frac{\partial u_z}{\partial r} \right) + \frac{\partial w}{\partial z} \frac{\partial u_z}{\partial z} \right) d\Omega, \\ a'(w; u_r) &= \int_{\Omega_1} v w \frac{u_r}{r^2} d\Omega, \\ c(\mathbf{u}; w, u_r) &= \int_{\Omega} w \left( u_r \frac{\partial u_r}{\partial r} + u_z \frac{\partial u_r}{\partial z} \right) d\Omega, \\ c(\mathbf{u}; w, u_z) &= \int_{\Omega} w \left( u_r \frac{\partial u_z}{\partial r} + u_z \frac{\partial u_z}{\partial z} \right) d\Omega, \\ e(w, T) &= \int_{\Omega_1} w g \beta (T - T_{amb}) d\Omega, \\ f(\mathbf{u}; s, T) &= \int_{\Omega} s \left( u_r \frac{\partial T}{\partial r} + u_z \frac{\partial T}{\partial z} \right) d\Omega, \\ g(s, T) &= \int_{\Omega} \alpha \left( \frac{1}{r} \frac{\partial s}{\partial r} \left( r \frac{\partial T}{\partial r} \right) + \frac{\partial s}{\partial z} \frac{\partial T}{\partial z} \right) d\Omega, \\ h(s, q_c) &= \int_{\Omega} s \frac{Q}{\rho C_p} d\Omega, \\ j(s, q_k) &= \int_{\Omega} s \frac{Q}{k} d\Omega. \end{aligned} \quad (19)$$

Now we define finite dimensional spaces  $X^h \subset X$ ,  $M^h \subset M$  and  $Y^h \subset Y$  to perform the spatial discretization of Eqs. (16)–(18) by means of Galerkin finite element method. The Galerkin formulation is obtained by restricting the weak form (16)–(18) to the finite dimensional spaces, namely, find  $(u_r^h, 0, u_z^h, p^h) \in H^1(\Omega^h) \times L^2(\Omega^h)$  such that

$$\begin{aligned} d(\mathbf{u}^h, q^h) &= 0 \quad \forall q^h \in M^h, \\ a(w^h, u_r^h) + c(\mathbf{u}^h; w^h, u_r^h) + b(w^h, p^h) &= a'(w^h, u_r^h) \quad \forall w^h \in X^h, \\ a(w^h, u_z^h) + c(\mathbf{u}^h; w^h, u_z^h) + b(w^h, p^h) &= e(w^h, T^h) \quad \forall w^h \in X^h, \\ f(\mathbf{u}^h; s_1^h, T^h) + g(s_1^h, T^h) &= h(s_1^h, q_c^h) \quad \forall s_1^h \in Y^h, \\ g(s_2^h, T^h) &= j(s_2^h, q_k^h) \quad \forall s_2^h \in Y^h. \end{aligned} \quad (20)$$

At this stage, we have to view the computational domain  $\Omega$  discretized into elements  $\Omega^e$ ,  $1 \leq e \leq n_{el}$ . Quadratic triangular finite elements are used to approximate the computational domain.

$$\begin{aligned}
 \mathbf{u}^h &= \sum_K N_K \mathbf{u}_K + \sum_{KD} N_K \mathbf{u}_{KD}, \\
 p^h &= \sum_K N_K p_K + \sum_{KD} N_K p_{KD}, \\
 T^h &= \sum_K N_K T_K + \sum_{KD} N_K T_{KD}.
 \end{aligned}
 \tag{21}$$

where  $N_K$  is the shape function associated with the node number  $K$  and  $\mathbf{u}_K, p_K$  and  $T_K$  are nodal unknowns. Moreover, the test functions  $w^h, q^h, s_1^h$  and  $s_2^h$  are taken as the span of shape functions. Then after substitution of (21) into (20), we obtain the discrete weak form as

$$\begin{aligned}
 \sum_I d(N_I, N_K) \mathbf{u}_I &= 0, \\
 \sum_I [a(N_I, N_K) + c(\mathbf{u}; N_I, N_K) + b(N_I, N_K)[\mathbf{u}_I, p_I]] &= a'(N_I, N_K), \\
 \sum_I [f(\mathbf{u}; N_I, N_K) + g(N_I, N_K)][\mathbf{u}_I, T_I] &= h(N_I, N_K), \\
 \sum_I [g(N_I, N_K)][\mathbf{u}_I, T_I] &= j(N_I, N_K).
 \end{aligned}
 \tag{22}$$

Assembling the element contributions to the weak form (22), we obtain the algebraic system governing nodal values of the discrete solution of the problem. Then the system takes the following form:

$$\begin{aligned}
 [\mathbf{A}][\mathbf{u}]' &= \mathbf{0}, \\
 [(\mathbf{B} + \mathbf{C}), \mathbf{P}][\mathbf{u}, p]' &= \mathbf{D}, \\
 [\mathbf{E}, \mathbf{F}][\mathbf{u}, T]' &= \mathbf{G}, \\
 [\mathbf{H}][T]' &= \mathbf{J}.
 \end{aligned}
 \tag{23}$$

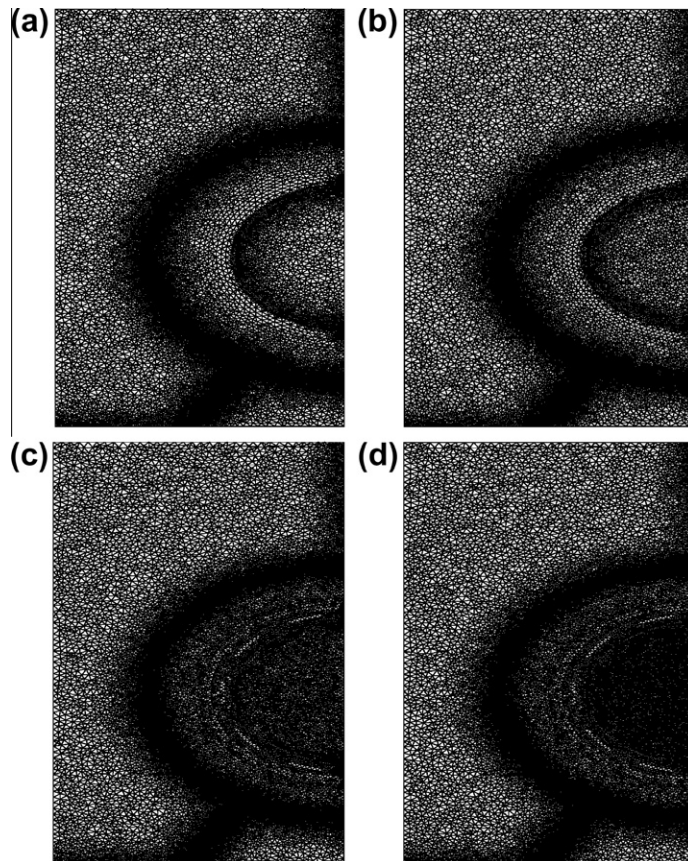


**Fig. 5.** Computational meshes: (a) mesh1 (13,487 nodes and 26,644 elements), (b) mesh2 (13,719 nodes and 27,104 elements), (c) mesh3 (14,919 nodes and 29,491 elements), and (d) mesh4 (15,724 nodes and 31,091 elements).

where  $\mathbf{u}$ ,  $p$  and  $T$  are the vector of unknown nodal values while  $B$ ,  $C$  and  $P$  are convection, diffusion and pressure gradient matrices. These matrices are obtained by evaluation of topological assembly of element contributions. The finite element matrices in left hand side of (23) are assembled to a single global matrix. If global matrix is non-singular then solution to the problem is uniquely defined. Since non linear terms are involved in convection matrices, iterative methods are used to solve the system (23). Stationary non linear solver is used to convert non-linear problem into the linear matrix system. Direct UMFPACK, a linear solver, is implemented to solve the linear matrix system for faster convergent solution. Once the auxiliary solution  $(\mathbf{u}^a, p^a, T^a)$  is obtained then the iterative scheme as follows:

$$(\mathbf{u}^{n+a}, p^{n+a}, T^{n+a}) = \omega^n(\mathbf{u}^n, p^n, T^n) + (1 - \omega^n)(\mathbf{u}^a, p^a, T^a), \tag{24}$$

where ‘ $n$ ’ is the iteration number and ‘ $a$ ’ represents the number of iterative steps required to obtain six decimal auxiliary solution. As the parameter  $\omega$  approaches to 1, the solution is convergent.

**4. Results and discussion**

First, we will present the concept of mesh sensitivity based on the fact that solution perturbation due to mesh refinement. The factors which influence surface temperature uniformity of the spherical cavity are investigated by performing numerical simulation. Nusselt number correlations are provided against the Rayleigh number along the heated spherical cavity without the aperture. A preliminary study on the surface temperature uncertainty due to uncertainty in material property is presented at the end.

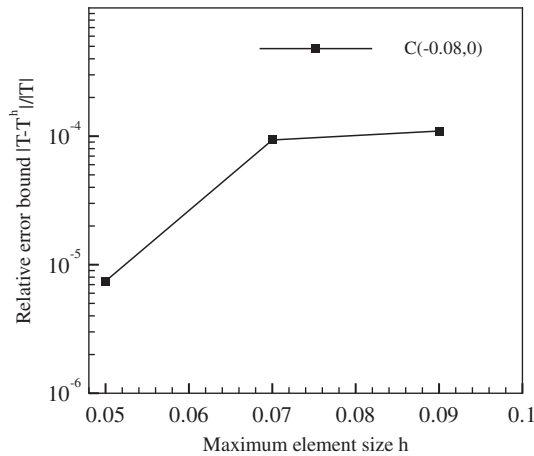


Fig. 6. Relative error bound vs maximum element size.

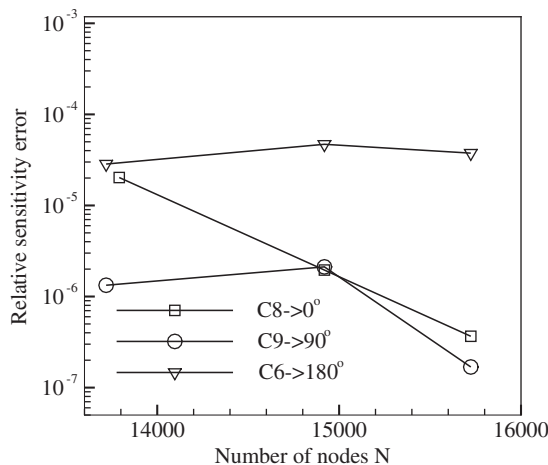


Fig. 7. Sensitivity of meshes at points C8 (0°), C9 (90°) and C6 (180°).

4.1. Mesh sensitivity analysis

Since the geometry of the furnace is complex, grid independence study for an accurate mesh does not work well. For this purpose, sensitivity of the mesh at a particular point is investigated to choose the best computational non uniform grid for finite element simulation. The basic idea is that solution at a particular point is perturbed due to refinement of the mesh. We start with a coarser mesh composed of 13,487 nodes by taking the maximum element size 0.09 m employed on each sub domain. Numerical simulation is performed and examined temperature gradients in regions of the computational domain to determine at which region should be more refined. It is observed that temperature gradients are steep in the narrow regions while they are very low in the wide regions.

Four non-uniform meshes 13,487 nodes (coarser mesh), 13,719 nodes (refine mesh), 14,919 nodes (finer mesh) and 15,724 nodes (very finer mesh) are employed on the computational domain and are shown in Fig. 5. We start with an assumption that  $T$  be the solution of a finer mesh and  $T^h$  be the solution of a mesh with maximum element size  $h$ . Then a relative error bound is defined as  $\max \left| \frac{T-T^h}{T} \right|$ . A point  $C (-0.08, 0)$  is chosen in the innermost region of the computational domain to study the mesh sensitivity. A schematic plot of the maximum element size against the relative error bound is presented in Fig. 6. From the plot, it clears that relative error bound increases as  $h$  increases. This point wise study prompted the local mesh refinement. In order to establish a reasonable mesh for the finite element simulation with faster convergence, a sensitivity error formula is incorporated with prescribed tolerance ( $10^{-6}$ ). Relative sensitivity error is defined as

$$|S^n| = |T^n - T^{n-1}| / |T^n|, \quad n = 1, 2, 3. \tag{25}$$

where  $T^0$  is temperature at a particular point in the computational domain for a coarser mesh and  $T^1$  is temperature at the same point for the next refined mesh (13,719 nodes and 27,104 elements).

The relative sensitivity errors are computed at points C8(0°), C9(90°) and C6(180°) and are plotted against the number of nodes in Fig. 7. Relative sensitivity error decreases as the number of nodes increases and finally satisfy the tolerance at C8

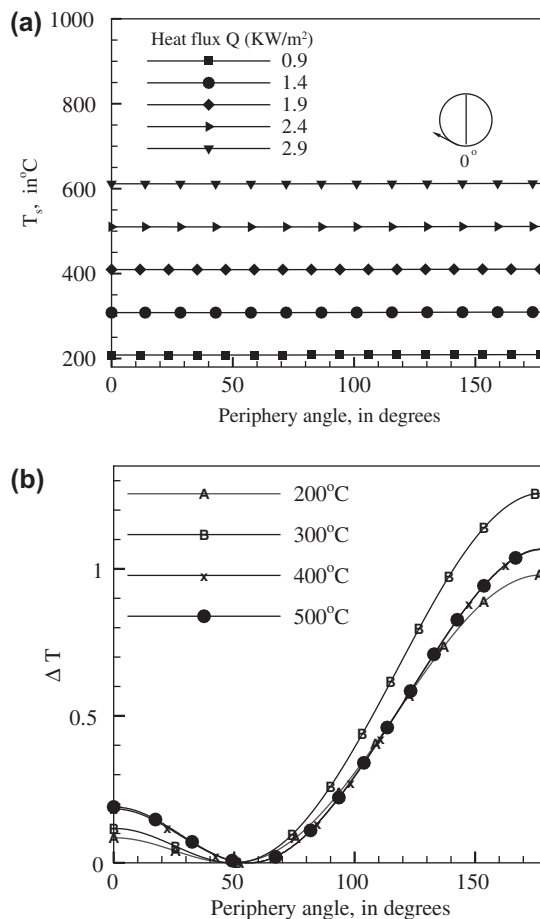
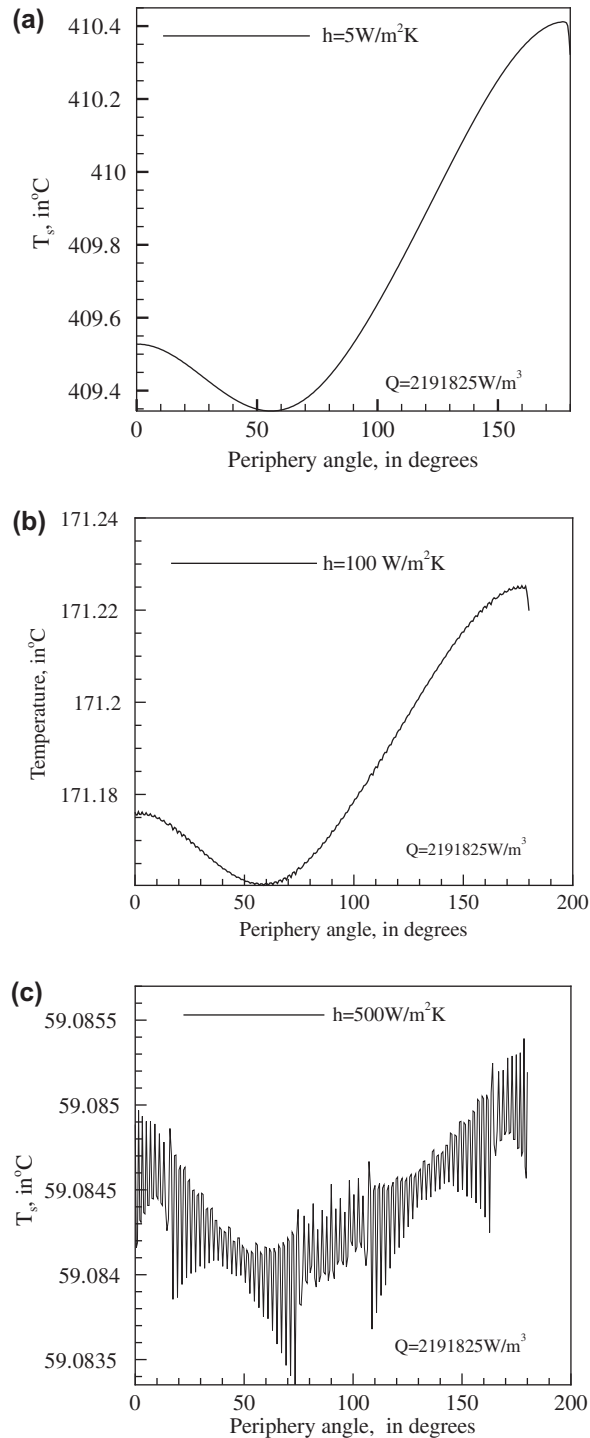


Fig. 8. (a) Temperature distribution and (b) temperature uniformity at various values of the cavity temperature.

and C9. At the position C6, relative sensitivity error does not satisfy inequality as the number of nodes increases due to formation of the convection plumelet. For instance,  $S^1 = 1.33 \times 10^{-6} > 10^{-6}$  for 13,719 nodes,  $S^2 = 2.11 \times 10^{-6} > 10^{-6}$  for 14,919 nodes and  $S^3 = 1.68 \times 10^{-7} < 10^{-6}$ . Therefore, the best reasonable mesh for finite element numerical simulation is that mesh composed of 15,724 nodes.



**Fig. 9.** Temperature profiles along boundary of the cavity for various values of convective heat transfer coefficient: (a)  $h = 5 \text{ W/m}^2\text{K}$ , (b)  $h = 500 \text{ W/m}^2\text{K}$  and (c)  $h = 1000 \text{ W/m}^2\text{K}$ .

#### 4.2. Surface temperature uniformity

The peripheral temperature distribution on the spherical cavity surface [the boundary common to ceramic (solid domain) and air.293 K (gas domain)] at various values of input heat flux are sketched in Fig. 8(a). From the plot, it is observed that surface temperature has a minimum value at the bottom stagnation point ( $0^\circ$ ) and increases to a maximum value at the top ( $180^\circ$ ). The reason for this is the influence of the boundary layer that starts to develop at the bottom and covers the surface till the occurrence of plumelets at the top. Maximum and minimum values of surface temperature increases with the increase of input heat flux up to certain level and then starts oscillating due to convection.

It is important to note that cavity attains particular temperature in the numerical simulation only when the experiment temperature at C9 and the simulation temperature at that point are the same. We define surface temperature uniformity along the peripheral boundary as  $\Delta T = T_{true} - T_{min}$  wherein  $T_{true}$  is the actual temperature and  $T_{min}$  is the minimum surface temperature recorded in the numerical simulation. The schematic sketch of the surface temperature uniformity along a cavity peripheral boundary is presented in Fig. 8(b). From the plot, it is observed that  $\Delta T$  is maximum at the surface top and minimum at the surface bottom of the cavity. Another important conclusion is that the value of  $\Delta T$  decreases along peripheral boundary as the cavity temperature increases.

Impact of convective heat transfer coefficient ( $h$ ) on the surface uniformity is systematically sketched in Fig. 9. At  $h = 25 \text{ W/m}^2 \text{ K}$ , there is slight temperature fluctuations along peripheral boundary of the Saturn which is not visible. At  $h = 100 \text{ W/m}^2 \text{ K}$ , temperature fluctuations are further intensified and at the same time  $\Delta T$  is gradually reduced. However, numerical computation results predicted that convective heat transfer coefficient  $h$  lies in between  $5 \text{ W/m}^2 \text{ K}$  and  $10 \text{ W/m}^2 \text{ K}$ .

Cavity emissivity depends on the temperature profile and geometric conditions. Emissivity is the ratio of the radiation emitted by cavity to the radiation emitted by the black body cavity. A schematic plot of the temperature profiles on the cavity surface at various values of emissivity  $\epsilon$  is shown in Fig. 10(a). From the plot, it is observed that the cavity surface temperature decreases as the emissivity increases at the same input heat flux. The effect of emissivity on the surface

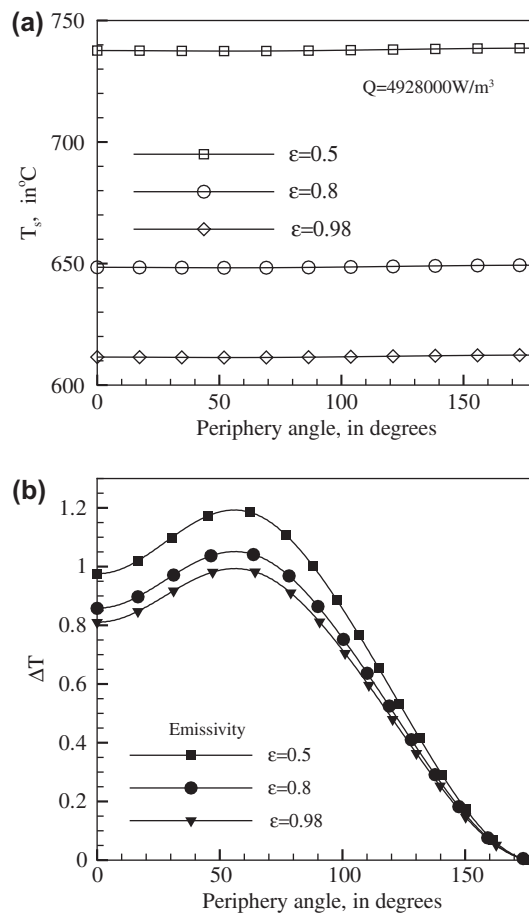


Fig. 10. (a) Surface temperature distribution and (b) surface temperature uniformity along peripheral boundary of the cavity at emissivity values ( $\epsilon$ ) 0.5, 0.8 and 0.98.

temperature uniformity is systematically sketched in Fig. 10(b). From the plot, it clears that surface temperature uniformity decreases as the cavity emissivity increases.

Numerical simulation results and experiment results at thermocouple positions C8(0°), C9(90°) and C6(180°) are compared and presented in terms of temperature profiles at various values of the cavity temperatures in Fig. 11. Agreement between experiment results and numerical simulation results is good at the top half of the cavity (from 90° to 180°) while there is significant deviation from the experiment at the bottom half.

4.3. Free convection characteristics of isothermal spherical cavity surface

Local Nusselt number distribution along peripheral boundary of the cavity is schematically sketched in Fig. 12(a). From the plot, local Nusselt number is maximum in between 0° and 90° and it is minimum in between 90° and 180°. Nusselt number is used to determine convective heat flux over conduction in steady state. The average Nusselt number along the curved peripheral boundary, subjected to uniform heat flux, is as follows.

$$Nu_{avg} = \frac{q'D}{k_f(T_s - T_{amb})}, \tag{26}$$

where  $q'$  is average heat flux,  $D$  is diameter of the sphere and  $k_f$  is thermal conductivity at the film temperature. Variation of average Nusselt number is plotted as a function of the Rayleigh number based on temperature difference,  $T_s - T_{amb}$ , in Fig. 12(b). From the plot, it clears that the slope of  $Nu_{avg} - Ra$  curve, at steady state, is about 0.18. This means that average Nusselt number correlates well with  $Ra^{0.18}$ , but a slight difference with an isothermal elliptic cavity (slope 0.25). It concludes that convection is dominant on the spherical cavity surface rather than the elliptic cavity surface.

4.4. Standard numerical temperature uncertainty

Thermal conductivity  $k$  is a material property which influences surface temperature uniformity ( $\Delta T$ ) and proportional to dissipation of heat. Better the insulation, lesser the heat dissipation. Standard numerical temperature uncertainty due to variation in thermal conductivity  $k$  at the three thermocouple positions C8(0°), C9(90°) and C6(180°) (see Fig. 2) systematically computed and presented in Table 1. We start with an assumption that representation of solution temperature on the surface  $T = T(r, z, k)$ . Temperature uncertainty  $u(T)$  at a calibrated position  $(r_i, z_i)$  is given by

$$u_i(T) = |c_i|u(k), \tag{27}$$

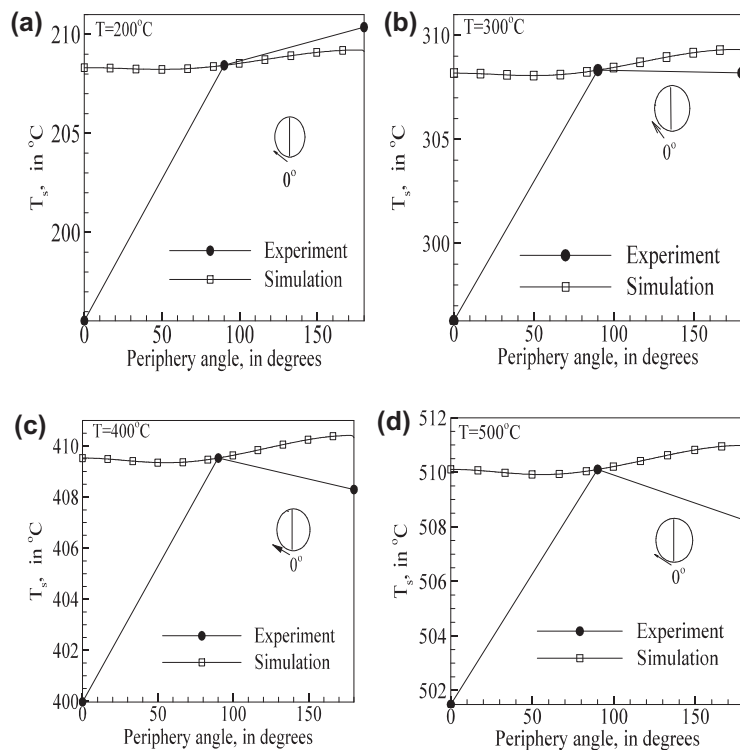
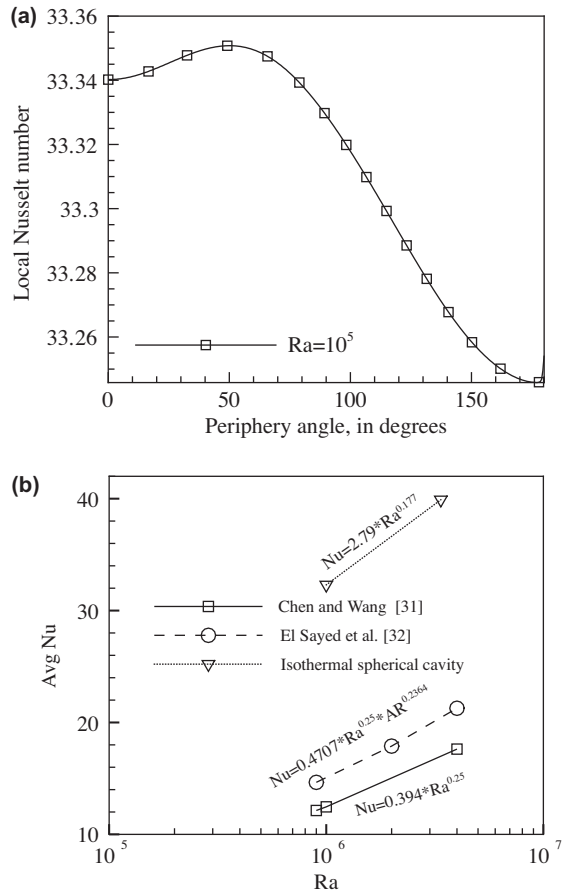


Fig. 11. Comparison of temperature profiles at various values of cavity surface temperature.



**Fig. 12.** (a) Local Nusselt number distribution along peripheral boundary of the cavity. (b) Average Nusselt number comparison against the Rayleigh number for isothermal surfaces.

**Table 1**  
Standard numerical surface temperature uncertainty along boundary of the spherical cavity.

Position	$k = 1.4$ Ceramic	$u(k)$	$T$ in °C	$(\Delta T_i)$	$c_i \frac{\Delta T}{2u(k)}$	$u_i(T)$
$C_9$	$k$	0.14	611.520642	3.836228	13.70081	1.918114
	$k + 10\%k$		609.683714			
	$k - 10\%k$		613.519942			
$C_8$	$k$	0.14	611.527482	3.839376	13.71206	1.919668
	$k + 10\%k$		609.688855			
	$k - 10\%k$		613.528231			
$C_6$	$k$	0.14	612.25629	3.664401	13.08715	1.832201
	$k + 10\%k$		610.503991			
	$k - 10\%k$		614.168392			

where  $u(k)$  is uncertainty in thermal conductivity  $k$ . The sensitivity coefficient,  $c_i$ , describes the extent to which the temperature  $T$  is influenced by variations in thermal conductivity  $k$ .

$$c_i = \frac{\Delta T}{\Delta k} \quad (\text{numerical}). \tag{28}$$

Combined calibration uncertainty  $u(T)$  is given by

$$u^2(T) = \sum_{i=1}^3 u_i^2(T). \tag{29}$$

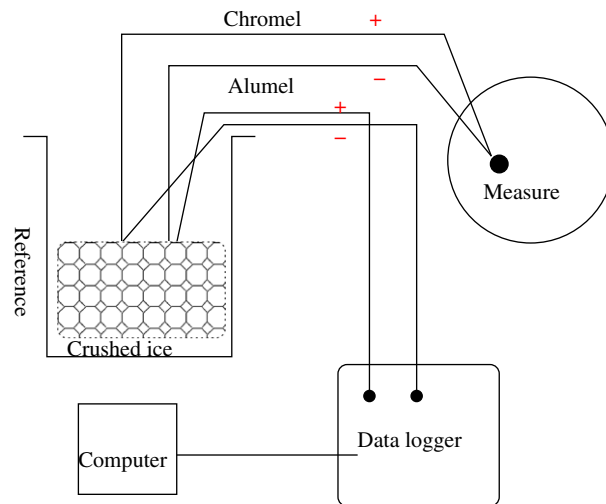


Fig. 13. Type *K* thermocouple calibration experiment set-up.

From (29), the calculated combined calibration uncertainty is 3.374343. Hence the expanded uncertainty  $U = Ku(T) = 2 \times 3.374343 = 6.548686$  (coverage factor  $K$  is chosen as 2). Temperatures reported at C8 (0°), C9 (90°) and C6(180°) on the cavity surface are  $611.527482 \pm 6.548686$  °C,  $611.520642 \pm 6.548686$  °C and  $612.25629 \pm 6.548686$  °C, respectively.

Therefore, 10% uncertainty in thermal conductivity of ceramic propagated 1% uncertainty in surface temperature when the cavity temperature is 600 °C.

## 5. Experiment procedure

In the experiment, temperature measurement at the nine calibrated positions on the surface of the spherical cavity using type *K* thermocouple calibration procedure and is schematically sketched in Fig. 13. The type *K* thermocouple [38] consists of the two wires of different metals chromel and alumel. The chromel has yellow insulation and is positive lead while the alumel has red insulation and is negative lead. One end of tips of the type *K* thermocouple are joined and established at the calibrated position (measure junction) of the spherical cavity. And tips of the other end is inserted in a container called the reference junction. Water and ice are at equal proportion in a container so that the reference junction temperature is maintained at 0 °C. Thermocouple, not of the type *K*, is used to connect the data logger and the reference junction, that forms closed loop. Then voltage is produced across the data logger by Seebeck principle.

The signal read by thermocouple returns temperature signal in terms of the potential difference ( $\delta V$ ). But this is actually a temperature difference ( $\delta T$ ) between the measure junction and the reference junction. Hence  $\delta V = \delta T = T$  at hot junction -  $T$  at reference junction =  $T_i - 0 = T_i$ . Therefore, temperature at the calibrated position is same as the temperature difference between tips of both ends. As a matter of fact, the thermocouple temperature obtained is expressed in volts. The surface temperature in volts converted to Celsius degrees using type *K* calibration inversion coefficients published in the literature.

## 6. Conclusions

Axi symmetric 2D numerical study has been carried out for the calibration furnace with the active central helicoidal block heating in an enclosure. In view of results and discussions presented, the following main conclusions are drawn.

- The best reasonable mesh for computation has been investigated using mesh sensitivity analysis. The observations are (1) relative error bound increases as the mesh maximum element size increases (2) relative sensitivity error decreases as the number of nodes increases.
- Cavity surface temperature recorded a minimum value at C8(0°) and a maximum value at C6(180°). Therefore, qualitative character of the heat transfer for the experiment and the numerical simulation remain the same.
- Surface temperature uniformity has been numerically investigated for various values of the convective heat transfer coefficient and various values of emissivity.
- Average Nusselt number is well correlated with the Rayleigh number  $Ra^{0.18}$  and compared with the published data.
- Standard numerical temperature uncertainty due to variation in thermal conductivity at specified positions on the cavity surface has been reported.

## Acknowledgement

The corresponding author is indebted to the Italian Ministry of University and Research for their financial support and very much thankful to Marco Dell'Isola, Andrea Frattolillo and Fausto Arpino for their constant encouragement and rigorous discussions during the entire part of the work.

## References

- [1] D. Nutter, D.P. Dewitt (Eds.), *Theory and Practise of Radiation Thermometry*, John Wiley and Sons, New York, 1989.
- [2] S.J. Cogan, K. Ryan, G.J. Sheard, The effects of vortex breakdown bubbles in the mixing environment inside a base driven bioreactor, *Appl. Math. Model.* 35 (2011) 1628–1637.
- [3] A. Riahi, J.H. Curvan, Full 3D finite element cosserat formulation with application in layered structures, *Appl. Math. Model.* 33 (2009) 3450–3464.
- [4] A.V. Phan, L. Baron, J.R.R. Mayor, G. Cloutier, Finite element and experimental studies of diametral error in cantilever bar turning, *Appl. Math. Model.* 27 (2003) 221–232.
- [5] O.O. Oluwole, P.O. Atanda, B.I. Imasogie, Finite element modeling of heat transfer in salt bath furnaces, *J. Miner. Mater. Charact. Eng.* 8 (3) (2009) 209–236.
- [6] A. Fournier, H.P. Bunge, R. Hollerbach, J.P. Vilotte, Application of the spectral element method to the axi symmetric Navier Stokes equation, *Geophys. J. Int.* 156 (2004) 682–700.
- [7] K.H. Chan, K. Zhang, J. Zou, G. Schubert, A non-linear, 3-D spherical  $\alpha^2$  dynamo using a finite element method, *Phys. Earth Planet. Int.* 128 (2001) 35–50.
- [8] F. Assous, P. Ciarlet Jr., S. Lebrunin, Theoretical tools to solve the axi symmetric Maxwell equations, *Math. Methods Appl. Sci.* 25 (2002) 49–78.
- [9] F. Assous, P. Ciarlet Jr., S. Lebrunin, J. Segree, Numerical solution to the time dependent Maxwell equations in axi symmetric singular domains: the singular complement method, *J. Comput. Phys.* 191 (2003) 147–176.
- [10] A. Bermudez, D. Gomez, M.C. Muniz, P. Salgado, Transient numerical solution of a thermo electrical problem in cylindrical induction heating furnaces, *Adv. Comput. Math.* 105 (2007) 217–247.
- [11] A. Bermudez, D. Gomez, M.C. Muniz, P. Salgado, A FEM/BEM for axi symmetric electromagnetic and thermal modeling of induction furnaces, *Int. J. Numer. Methods Eng.* 71 (2007) 856–878.
- [12] S. Li, L.R. Petzold, J.M. Hyman, *Solution Adaptive Mesh Refinement and Sensitivity Analysis for Parabolic Partial Differential Equation Systems*, USA.
- [13] R. Becker, B. Vexler, A posteriori error estimation for finite element discretizations of parameter identification problems, *Numer. Math.* 96 (3) (2004) 1–102.
- [14] R. Becker, B. Vexler, Mesh refinement and numerical sensitivity analysis for parameter calibration of partial differential equations, *J. Comput. Phys.* 206 (2005) 95–110.
- [15] T. Gratsch, K.J. Bathe, A posteriori error estimation techniques in practical finite element analysis, *J. Comput. Struct.* 83 (2005) 235–265.
- [16] P. Nithiarasu, O.C. Zienkiewicz, Adaptive mesh generation for fluid mechanics problems, *Int. J. Numer. Methods Eng.* 47 (2000) 629–662.
- [17] F. Kuznik, G. Rusaouen, Numerical prediction of natural convection occurring in building components: a double population Lattice Boltzmann method, *Numer. Heat Transfer, Part A* b52 (2007) 315–335.
- [18] W.R. Chen, Natural convection heat transfer between inner sphere and outer vertically eccentric cylinder, *Int. J. Heat Mass Transfer* 53 (23–24) (2010) 5147–5155.
- [19] A. Prhashanna, R.P. Chhabra, Free convection in power-law fluids from a heated sphere, *Chem. Eng. Sci.* 65 (23) (2010) 6190–6205.
- [20] M.Z. Salleh, R. Nazar, I. Pop, Modeling of free convection boundary layer flow on a solid sphere with Newtonian heating, *Acta Appl. Math.* 112 (3) (2010) 263–274.
- [21] M. Miraj, M.A. Alim, M.A.H. Mamun, Effect of radiation on natural convection flow on a sphere in presence of heat generation, *Int. Commun. Heat Mass Transfer* 37 (6) (2010) 660–665.
- [22] P. Bagchi, K. Kottam, Effects of freestream isotropic turbulence on heat transfer from a sphere, *Phys. Fluids* 20 (7) (2008).
- [23] S. Yang, V. Raghavan, G. Gogos, Numerical study of transient laminar natural convection over an isothermal sphere, *Int. J. Heat Fluid Flow* 28 (4) (2007) 821–837.
- [24] B. Gebhart, Y. Jaluria, R.L. Mahajan, B. Sammakia, *Buoyancy Induced Flows and Transport*, New York, 1988.
- [25] J.N. Arnold, I. Cotton, D.K. Edwards, Experimental investigation of natural convection in inclined rectangular regions of different aspect ratios, *ASME J. Heat Transfer* (1975).
- [26] S.M. Bajorek, J.R. Lloyd, Experimental investigation of natural convection in partitioned enclosures, *J. Heat Transfer* 104 (1982) 527–532.
- [27] P.S. Ayyaswamy, I. Cotton, The boundary layer regime for natural convection in a differentially heated, tilted rectangular cavity, *J. Heat Transfer* 95 (1973) 543–545.
- [28] S. Ostrach, Natural convection in enclosures, *Adv. Heat Transfer*, New York 8 (1972) 161–227.
- [29] S. Matle, S. Sundar, A 2D Numerical study on aspect ratio of the enclosure and aperture heat losses for the high temperature spherical furnace using FEM, *IJAM* 24 (2) (2011) 267–289.
- [30] R. Anderson, G. Lauriat, The horizontal natural convection boundary layer regime in a closed cavity, *SERI/TP-252-2830*, Sol. Energy Res. Inst., Golden, Colorado, Proc. Int. Conf. Heat Transfer 4 (1986) 1453–1458.
- [31] Y.M. Chen, K.C. Wang, J. Chin. *Inst. Eng.* 27 (1996) 353.
- [32] A.O. Elsayed, E.Z. Ibrahim, S.A. Elsayed, Free convection from a constant heat flux elliptic tube, *Energy Conserv. Manage.* 44 (2003) 2445–2453.
- [33] A. Bejan, C.L. Tien, Laminar natural convection heat transfer in a horizontal cavity with different end temperatures, *J. Heat Transfer* 100 (1978) 641–647.
- [34] A. Bejan, *Convection Heat Transfer*, second ed., Wiley, New York, 1995.
- [35] European Cooperation and Accreditation Laboratory Task Force, Expression of the uncertainty of measurement in calibration, *Guide to ISO 13005*, 1990.
- [36] J. Drnovsek, J. Bojkovski, I. Pusnik, Analysis of equalising blocks in calibration of thermometers, *Measurement* 23 (1998) 145–150.
- [37] C. Bernardi, M. Dauge, Y. Maday, *Spectral Methods for Axi Symmetric Domains*, Numerical Algorithms and Tests due to Mejdji, Azarez, 1999.
- [38] Bentley, R.E. (Ed.), *Theory and Practise of Thermoelectric Thermometry*, 1998.